Nonadiabatic photodissociation dynamics of *ICN* in the *Ã* continuum: A semiclassical initial value representation study

Eduardo A. Coronado, Victor S. Batista, and William H. Miller
Department of Chemistry, University of California, and Chemical Sciences Division, Lawrence Berkeley National Laboratory, Berkeley, California 94720

In this paper we investigate the nonadiabatic photodissociation dynamics of *ICN* in the *Ã* continuum, using a semiclassical initial value representation method which is able to describe electronically nonadiabatic processes through the quantization of the classical electron–nuclear model Hamiltonian of Meyer and Miller [J. Chem. Phys. **70**, 3214 (1979)]. We explore the capabilities of this semiclassical technique as applied to studying the *ICN* absorption spectrum, and the *CN* rotational distribution, through direct comparison of our semiclassical results with experimental data, and with full quantum mechanical calculations. We find that the Meyer–Miller Hamiltonian, quantized according to the semiclassical prescription, describes the *ICN* photodissociation dynamics in excellent agreement with full-quantum mechanical calculations. © *2000 American Institute of Physics.* [S0021-9606(00)01113-2]

I. INTRODUCTION

Understanding the effect of electronic nonadiabatic transitions in the photodissociation dynamics of polyatomic systems is a fundamental problem of much current research interest in studies of chemical reaction dynamics. The effects of electronic relaxation processes on molecular photofragmentation dynamics are also ideally suited to detailed investigations using new computational methods for simulating chemical reactions. This paper reports the first application of semiclassical initial value representation (SC–IVR) methods[1–24] to study the effect of electronic nonadiabaticity in the state-to-state photofragmentation dynamics of *ICN* in the gas phase.

Experiments have shown that the *ICN* molecule has a broad continuum absorption in the 200–300 nm range (see Fig. 1). Photolysis of the *ICN* molecule at the peak of the *Ã* continuum (e.g., ~266 nm) produces two peaks in the translational photofragment spectra, which are assigned to two photodissociation pathways that produce iodine atoms in the $I(^2P_{1/2})$ and $I^*(^2P_{3/2})$ spin–orbit states, respectively, along with the *CN* radical in the ground electronic state $CN(X\,^2\Sigma^+)$, as indicated below,

$$ICN + \hbar\omega \rightarrow I^*(^2P_{1/2}) + CN(X\,^2\Sigma^+)$$
$$\rightarrow (^2P_{3/2}) + CN(X\,^2\Sigma^+), \qquad (1.1)$$
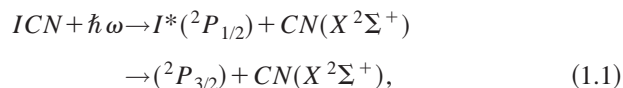
where $\hbar\omega$ is the photoexcitation energy. Little vibrational excitation is found in the *CN* fragment ($>98\%$ in $\nu=0$), but the rotational distribution of *CN* involves highly excited states and exhibits a bimodal structure (see Fig. 2). The *CN* fragment is formed rotationally cold—i.e., with rotational distributions that peak at low quantum numbers—when dissociation of the molecule produces excited state iodine atoms $I^*(^2P_{1/2})$, while the channel forming ground state iodine $I(^2P_{3/2})$ produces rotationally hot *CN* fragments. Experiments have also shown that the I/I^* branching ratio in the

CN rotational distribution is not very sensitive to the initial temperature of the parent molecule but strongly wavelength dependent, with I^* production accounting for approximately 62% of the total product at 266 nm, but much less at both lower and higher photoexcitation energies.[25]

Much of the earlier experimental and theoretical work developed for understanding the photodissociation dynamics of *ICN* via its *Ã* continuum has been summarized by Tannor, Morokuma and co-workers,[26–28] who carried out rigorous time-dependent quantum dynamics simulations as well as *ab initio* calculations of the electronic excited state potential energy surfaces where nuclear and electronic relaxation dynamics takes place after photoexcitation of the system. Other theoretical studies of the *ICN* photodissociation dynamics can be found in Refs. 29–31.

Exact quantum dynamical methods have also made significant progress in the understanding of many other chemical reactions.[32] However, these rigorous computational techniques are currently limited to systems with only a few degrees of freedom, since they usually require computational effort and storage space that scales exponentially with the number of coupled degrees of freedom. The extensively investigated *ICN* photodissociation reaction is therefore, ideal to explore the capabilities of alternative computational methods to model excited state quantum reaction dynamics.

Since classical trajectory methods have been extremely successful for describing diabatic dynamics of molecular systems with many degrees of freedom, it is natural to try to extend such approaches to treat nonadiabatic dynamics involving several potential energy surfaces. Approximate techniques for including nonadiabatic effects have been developed in terms of effective path methods,[33–40] and surface hopping algorithms[41–47] that were successfully implemented in various studies of ultrafast photodissociation dynamics.[48–54] However, the development of a rigorous method for generalizing classical molecular dynamics tech-
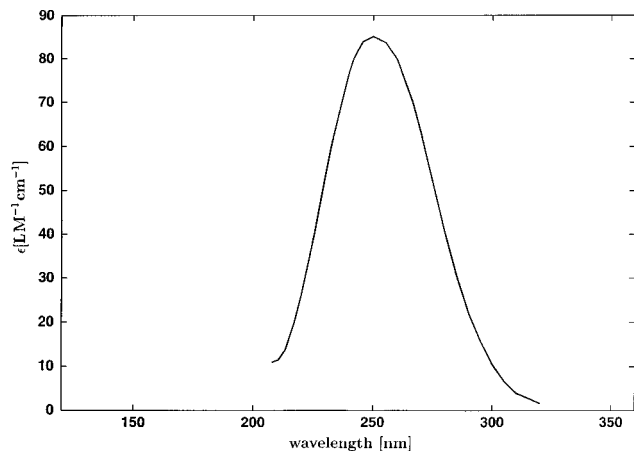
FIG. 1. Experimental *ICN* absorption spectrum (Ref. 76).

niques to incorporate quantum mechanical effects correctly is still a goal of current investigations.

    Early theoretical studies of *ICN* photodissociation dynamics were focused on interpreting the cold vibrational distributions of *CN* fragments using collinear models.[55–58] More recently, classical molecular dynamics (MD) simulations were also carried out to obtain the rotational distribution of *CN* fragments using various model potential energy surfaces. In general, classical MD simulations studies that included the description of nonadiabatic effects were based on the Meyer–Miller classical-analog method in an assumed diabatic basis set representation.[28,59,60]

    The classical analog-model[33] is an effective path method that propagates electronic and nuclear degrees of freedom according to classical equations of motion, and accounts for the multiple surfaces by means of an average potential.[34] Guo and Schatz tested the validity of the classical-analog method for describing the *ICN* photodissociation dynamics by comparing its results with accurate quantum mechanical results obtained by solving the time-independent Schrödinger equation for the excited state scattering wave function.[60] These calculations were carried out using empiri-
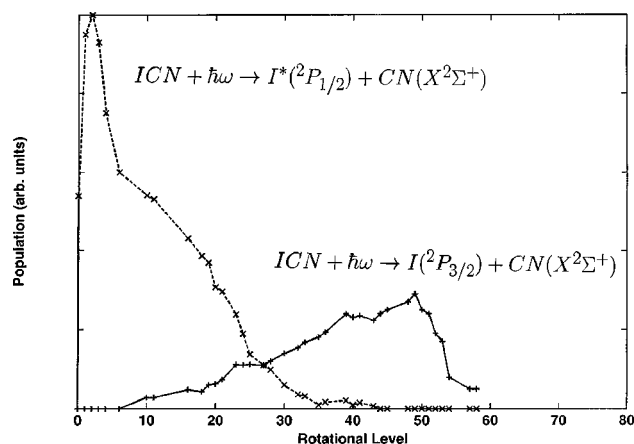

FIG. 2. Experimental *CN* rotational distributions associated with two possible photofragmentation channels as described in the text. Experimental data was obtained from low resolution LIF spectra after 266 nm photolysis of 300 K *ICN* (Ref. 77). $\hbar\omega$ is the photoexcitation energy.
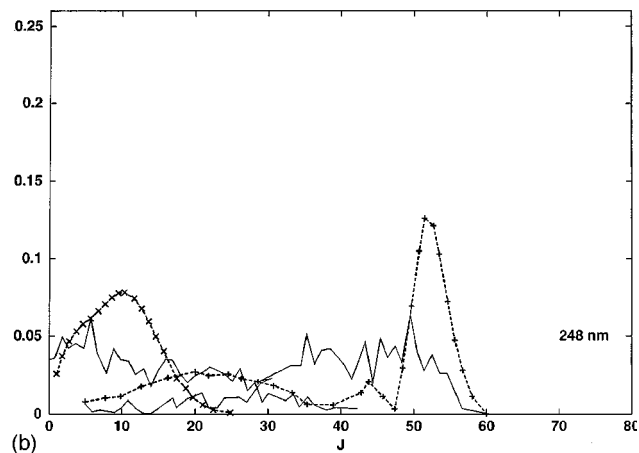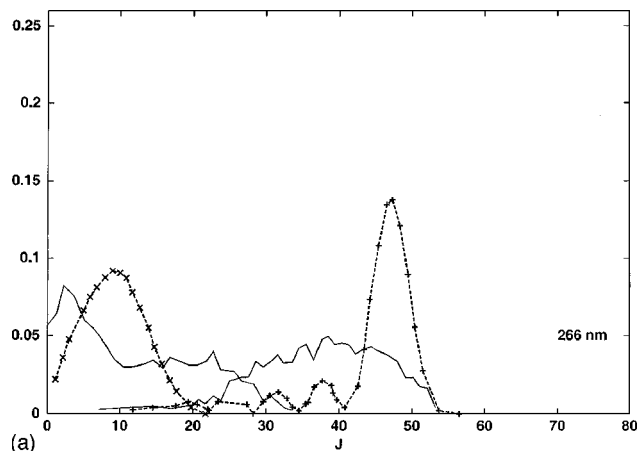

FIG. 3. Comparison between quantum (symbols) and classical-analog calculations (solid lines) for the *CN* rotational distributions in the *I* and *I** channels, individually normalized, adapted from Ref. 60. (a) 266 nm; (b) 248 nm.

cal potential energy surfaces developed by Goldfield *et al.* in an early study of *ICN* photodissociation dynamics in terms of the Meyer–Miller classical-analog method.[59] From the comparison with full-quantum mechanical results for the *I*/*I** quantum yields, the bimodal rotational distribution, and the total cross section, Guo and Schatz concluded that the classical-analog calculations were not accurate enough to describe the *ICN* photodissociation dynamics properly, probably due to the inherent weakness of the Meyer–Miller method where trajectories were governed by an average potential even in the asymptotic region (see Fig. 3).[60] In this paper we explore to what extent semiclassical quantization of the classical Meyer–Miller Hamiltonian is able to overcome the shortcomings of the totally classical formulation, by incorporating nuclear coherence and interference effects within the description of the SC–IVR.

    The SC–IVR is a generalization of classical molecular dynamics simulation methods that combines the quantum superposition of probability amplitudes with real-valued classical trajectories in the computation of the quantum mechanical propagator.[1] In recent years there has been a rebirth of interest for developing new implementation methodologies of these approaches, including the Herman–Kluk (HK) SC–IVR,[12] the linearized (L)SC–IVR method,[61–64] the time

average approach,[65] and forward–backward (FB)SC–IVR techniques.[3,66,67] These methods aim to provide a more tractable alternative to exact quantum mechanical methods for dynamics calculations as well as an intuitive understanding of complex quantum dynamics associated with chemical reactions in terms of classical mechanics, but where quantum coherence effects are included correctly and naturally. The comparison with state specific quantum mechanical results, presented in this paper, provides perhaps the most detailed and rigorous possible test of these new SC–IVR techniques for simulating nonadiabatic excited state photofragmentation dynamics of a real polyatomic system.

The semiclassical methodology implemented in this paper removes the drawbacks inherent in the classical version of the Meyer–Miller approach. It has been successfully tested for the three one-dimensional model problems suggested by Tully for testing nonadiabatic dynamics,[41] and for the spin-boson model for dissipative systems.[68,69] However, the only application to date for a real molecular system has been our nonadiabatic MD simulation of the ultrafast photodissociation dynamics of ozone.[2] In that work the semiclassical methodology was implemented on *ab initio* potential energy surfaces and the photofragmentation dynamics was simulated on the lower lying excited states of $^1A''$ symmetry that are coupled by a conical intersection. The capabilities of the SC–IVR were demonstrated for simulating the Chappuis absorption band, by comparing our semiclassical results directly with experimental data, and with full-quantum mechanical calculations.

In this paper we extend our semiclassical calculations to compute not only the photoabsorption spectrum of *ICN*, but also the rotational distributions of *CN* photofragments and the asymptotic nuclear wave packet components that are even more demanding quantities. The rotational distribution provides a more detailed description of dynamics and is particularly challenging to calculate not only because it involves the evaluation of a high dimensional integral with an oscillatory integrand, but also because it is determined by the asymptotic shape of the nuclear wave packet components and is sensitive to how various different potential energy surfaces are populated according to the details of the electronic coupling between the excited electronic states and the speed with which the system moves through the coupling regions at the conical intersection. It is shown in this paper that the HK version of the SC–IVR methodology, together with stationary phase Monte Carlo methods, can be effectively implemented as described in Ref. 2 to obtain semiclassical results that are in excellent agreement with full-quantum mechanical calculations.

The paper is organized as follows. In Sec. II we first outline our semiclassical approach for modeling the photodissociation dynamics, the calculation of the absorption spectrum, and the rotational distributions of *CN* photofragments. Section III then summarizes our results and compares them with full-quantum calculations. Section IV summarizes and concludes.

II. METHODS

A. The semiclassical approach

The time-dependent wave function Ψ_t can be obtained from the initial state of the system Ψ_0 according to

$$\Psi_t(\mathbf{q}') = \int d\mathbf{q}\, K_t(\mathbf{q}',\mathbf{q})\Psi_0(\mathbf{q}), \qquad (2.1)$$

where $\mathbf{q}$ denotes the N coordinates of nuclear and electronic degrees of freedom collectively (*vide infra*), and the time dependent propagator $K_t(\mathbf{q}',\mathbf{q})$ is simply the evolution operator in coordinate representation,

$$K_t(\mathbf{q}',\mathbf{q}) \equiv \langle \mathbf{q}'|e^{-i\hat{H}t/\hbar}|\mathbf{q}\rangle. \qquad (2.2)$$

Here $\hat{H}$ is the Hamiltonian operator of the molecular system. The Herman–Kluk (HK),[12] or coherent state IVR for the time evolution operator, is

$$K_t^{HC}(\mathbf{q}',\mathbf{q}) = (2\pi\hbar)^{-N}\int_{-\infty}^{\infty} d\mathbf{p}_0 \int_{-\infty}^{\infty} d\mathbf{q}_0\, g_{q_t,p_t}(\mathbf{q}')$$
$$\times C_t(\mathbf{p}_0,\mathbf{q}_0)e^{iS_t(\mathbf{p}_0,\mathbf{q}_0)/\hbar}g_{\mathbf{q}_0,\mathbf{p}_0}(\mathbf{q})^*, \qquad (2.3)$$

where the integration variables $(\mathbf{p}_0,\mathbf{q}_0)$ in Eq. (2.3) are the initial conditions for classical trajectories; $\mathbf{q}_t \equiv \mathbf{q}_t(\mathbf{p}_0,\mathbf{q}_0)$ and $\mathbf{p}_t \equiv \mathbf{p}_t(\mathbf{p}_0,\mathbf{q}_0)$ are the time-evolved coordinates and momenta, and $S_t(\mathbf{p}_0,\mathbf{q}_0)$ the classical action along this trajectory, obtained by integrating the following equation:

$$\frac{dS_t}{dt} = \mathbf{p}_t \cdot \dot{\mathbf{q}}_t - H(\mathbf{p}_t,\mathbf{q}_t). \qquad (2.4)$$

along with the usual classical equations of motion,

$$\frac{dq(j)}{dt} = \frac{\partial H(\mathbf{q},\mathbf{p})}{\partial p(j)} \quad \text{and} \quad \frac{dp(j)}{dt} = -\frac{\partial H(\mathbf{q},\mathbf{p})}{\partial q(j)}. \qquad (2.5)$$

The Hamiltonian $H(\mathbf{p}_t,\mathbf{q}_t)$, in Eqs. (2.4) and (2.5) above, is the Meyer–Miller classical analog model for the system with total angular momentum $\mathbf{J}=0$.

$$H(R,K,\theta,l,\widetilde{\mathbf{p}},x) = \frac{K^2}{2M} + \frac{l^2}{2MR^2} + \frac{l^2}{2mr^2}$$
$$+ \frac{1}{2}\sum_{k=1}^{2}\sum_{k=1}^{2}[\widetilde{p}(k)\widetilde{p}(k')$$
$$+ x(k)x(k')]H_{k,k'}(R,\theta)$$
$$- \frac{1}{2}\sum_{k=1}^{2}H_{k,k}(R,\theta). \qquad (2.6)$$

written in terms of cartesian electronic degrees of freedom $(\mathbf{x},\widetilde{\mathbf{p}})$, and Jacobi nuclear coordinates (R,θ) and momenta (K,l), assuming the rigid rotor approximation for the *CN* fragment with equilibrium bond length r. As illustrated in Fig. 4, the Jacobi coordinate R is the distance between the iodine atom and the *CN* center of mass, and K is its corresponding momentum, Θ is the Jacobi angle, and l is its corresponding canonical conjugate variable. M and m, introduced by Eq. (2.6), are the $I-CN$ and $C-N$ reduced
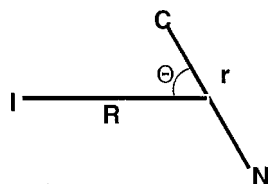
J. Chem. Phys., Vol. 112, No. 13, 1 April 2000

Nonadiabatic photodissociation dynamics   5569

FIG. 4. Definition of the Jacobi coordinates (R,Θ) for the ICN molecule. R is the distance between the iodine atom and the CN center of mass.

masses, respectively. The diabatic electronic Hamiltonian matrix elements $H_{k,k'}(R,\theta)$, in Eq. (2.6), are assumed to be real and symmetric.

The wave functions for the coherent states in Eq. (2.3) are given by

$$g_{\mathbf{q}_t,\mathbf{p}_t}(\mathbf{q}) = \prod_{j=1}^{N} \left(\frac{2\,\gamma(j)}{\pi}\right)^{1/4} \exp\left(-\gamma(j)[q(j)-q_t(j)]^2\right.$$
$$\left. + \frac{i}{\hbar}p_t(j)[q(j)-q_t(j)]\right), \qquad (2.7)$$

and similarly for $g_{\mathbf{q}_0,\mathbf{p}_0}(\mathbf{q})$. The Gaussian functions introduced by Eq. (2.7) are numerically convenient but not rigorously valid as functions of the Jacobi coordinates (R,Θ)—i.e., they are not periodic functions of Θ, and they extend to unphysical negative values of R. However, these functions are assumed to be sufficiently localized, so that the error introduced by this approximation is expected to be negligible.

The pre-exponential factor in the integrand of Eq. (2.3) is given by

$$C_t(\mathbf{p}_0,\mathbf{q}_0) = \sqrt{\det[\mathbf{M}]}, \qquad (2.8)$$

where $\mathbf{q} \equiv (R,\theta,\mathbf{x})$ and $\mathbf{p} \equiv (K,l,\bar{\mathbf{p}})$ denote the nuclear and electronic variables collectively, and $\mathbf{M}$ is a linear combination of components of the monodromy matrix,

$$M(j,k) = \frac{1}{2}\left(\frac{\partial q_t(k)}{\partial q_0(j)} + \frac{\gamma(j)}{\gamma(k)}\frac{\partial p_t(k)}{\partial p_0(j)} - \frac{1}{2i\hbar\,\gamma(k)}\frac{\partial p_t(k)}{\partial q_0(j)}\right.$$
$$\left. - 2i\hbar\,\gamma(j)\frac{\partial q_t(k)}{\partial p_0(j)}\right), \qquad (2.9)$$

where $\gamma(j)$ are the constant parameters in the Gaussian wave packets of Eq. (2.7). The various time dependent partial derivatives are obtained by numerical integration of the following equations for the stability matrix:

$$\frac{d}{dt}\left(\frac{\partial p_t(i)}{\partial z(j)}\right) = -\sum_{k=1}^{N}\left(\frac{\partial^2 H(\mathbf{p}_t,\mathbf{q}_t)}{\partial p_t(k)\partial q_t(i)}\frac{\partial p_t(k)}{\partial z(j)}\right.$$
$$\left. + \frac{\partial^2 H(\mathbf{p}_t,\mathbf{q}_t)}{\partial q_t(k)\partial q_t(i)}\frac{\partial q_t(k)}{\partial z(j)}\right),$$

$$\frac{d}{dt}\left(\frac{\partial q_t(i)}{\partial z(j)}\right) = +\sum_{k=1}^{N}\left(\frac{\partial^2 H(\mathbf{p}_t,\mathbf{q}_t)}{\partial p_t(k)\partial p_t(i)}\frac{\partial p_t(k)}{\partial z(j)}\right.$$
$$\left. + \frac{\partial^2 H(\mathbf{p}_t,\mathbf{q}_t)}{\partial q_t(k)\partial p_t(i)}\frac{\partial q_t(k)}{\partial z(j)}\right),$$

where $z = p_0$ or q_0.

The time-dependent nuclear wave function of electronic state k, $\Psi_t^k(R,\Theta)$, is obtained from the total time-dependent wave function $\Psi_t(\mathbf{x},R,\theta)$, by projecting out the corresponding electronic state ϕ^k,

$$\Psi_t^k(R,\theta) = \int d\mathbf{x}\langle\phi^k|\mathbf{x}\rangle\langle\mathbf{x},R,\theta|\Psi_t\rangle, \qquad (2.10)$$

with

$$\phi^k(\mathbf{x}) = x_k e^{-1/2(x_1^2+x_2^2)}. \qquad (2.11)$$

$\Psi_t(\mathbf{q})$, in Eq. (2.10), is obtained by substituting Eq. (2.3) into Eq. (2.1),

$$\Psi_t(\mathbf{q}) = (2\pi\hbar)^{-N}\int_{-\infty}^{\infty}d\mathbf{p}_0\int_{-\infty}^{\infty}d\mathbf{q}_0\,g_{\mathbf{q}_t,\mathbf{p}_t}(\mathbf{q})$$
$$\times C_t(\mathbf{p}_0,\mathbf{q}_0)e^{iS_t(\mathbf{p}_0,\mathbf{q}_0)/\hbar}\Psi^g(\mathbf{q}_0,\mathbf{p}_0), \qquad (2.12)$$

where $\Psi^g(\mathbf{q}_0,\mathbf{p}_0)$ is the coherent state transform of the initial wave function,

$$\Psi^g(\mathbf{q}_0,\mathbf{p}_0) = \int d\mathbf{q}'\,g_{p_0,q_0}(\mathbf{q}')^*\Psi_0(\mathbf{q}'). \qquad (2.13)$$

The total photoabsorption cross section $\sigma(\lambda)$, as a function of the photolysis wave length λ, is calculated by the Fourier transform of the survival amplitude $\xi(t)$

$$\sigma(\lambda) = \frac{1}{2\pi\hbar}\int_{-\infty}^{\infty}dt\,\xi(t)e^{i\omega t}, \qquad (2.14)$$

with $\omega = 2\pi c/\lambda$, and

$$\xi(t) \equiv \langle\Psi_0|e^{-i\hat{H}t/\hbar}|\Psi_0\rangle = \langle\Psi_0|\Psi_t\rangle, \qquad (2.15)$$

where Ψ_0 is the initial ground state wave function multiplied by the constant transition dipole moment (Condon approximation).

As presented above, the computational task is to evaluate a rather high dimensional phase space average over initial conditions defined as follows

$$\xi(t) = (2\pi\hbar)^{-N}\int_{-\infty}^{\infty}d\mathbf{p}_0\int_{-\infty}^{\infty}d\mathbf{q}_0\,\Psi^{g*}(\mathbf{q}_t,\mathbf{p}_t)$$
$$\times C_t(\mathbf{p}_0,\mathbf{q}_0)e^{iS_t(\mathbf{p}_0,\mathbf{q}_0)/\hbar}\Psi^g(\mathbf{q}_0,\mathbf{p}_0). \qquad (2.16)$$

In order to damp out the most oscillatory regions of the integrands, which make little contribution to the value of the integrals in Eqs. (2.12) and (2.16), we have utilized a simplified version of the Filinov,[70,71] or stationary phase Monte Carlo (SPMO) method,[72] which is described in Ref. 2.

The time evolved wave packet $\chi_t^J(K)$ in the $K-J$ representation (where K is the nuclear momentum and J is the rotational quantum number of CN), contains the rotational product distributions at all energies, and is given by

$$\chi_t^J(K) = A\int_0^{\infty}dR\int_0^{\pi}d\Theta\,Y_{J0}^*(\Theta)\sin(\Theta)e^{-iKR}\Psi_t^k(R,\Theta), \qquad (2.17)$$

where A is a normalization constant, and the spherical harmonic $Y_{J0}(\Theta)$ represents the Jth rotational state of the CN fragment in the plane of the ICN molecule. The rotational product distributions are obtained at different energies $\hbar\omega$ in

terms of the square of the asymptotic wave packet amplitude $\chi_t^J(K)$ along the different elliptical cuts defined as a function of K and J by the following formula:

$$E_i + \hbar\omega - E_0 = \frac{\hbar^2 K^2}{2M} + \frac{\hbar^2 J(J+1)}{2mr^2}, \tag{2.18}$$

where E_i is the initial energy of the wave function, ω is the photon energy, and E_0 is the asymptotic energy of the fragments.

B. Sample preparation and photoexcitation

In our simulations trajectories are initialized through MC sampling of coordinates and momenta according to localized phase space distributions determined by the coherent state transforms of the initial excited state wave functions, created under the assumption that the photolysis event promotes molecules instantaneously from the ground electronic state to the optically allowed excited states which are resonant with the excitation wavelength (Franck–Condon approximation).

We assume that the dominant contributions to the excited state relaxation dynamics result from parallel transitions from the ground state $^1\Sigma_0^+$ potential energy surface to the excited electronic state with $^3\Pi_0^+$ symmetry, and perpendicular transitions to the $^1\Pi_1$, and $^3\Pi_1$ excited electronic states. This assumption is based on *ab initio* calculations showing that the ratios of the transition intensities to the $^3\Pi_0^+$, $^1\Pi_1$, and $^3\Pi_1$ are 0.66:0.28 and 0.06, respectively.[28] *Ab initio* calculations also show that the $^3\Pi_0^+$ potential energy surface has an attractive well of about 0.45 eV at $R = 4.92$ a.u., and is significantly coupled only to the $^1\Pi_1$ excited state, by a conical intersection at $R = 6.42$ a.u. Therefore, in addition to the ground electronic state information, we include in our simulations the two excited state surfaces, $^3\Pi_0^+$ and $^1\Pi_1$, and the coupling between these two surfaces. In our simulations we calculate the values of the excited state potential energy surfaces and the couplings between them, according to analytic expressions taken from Ref. 73. Our simulations, therefore, model nonadiabatic dynamics on full *ab initio* potential energy surfaces without relying on any approximate model potential.

The nuclear wave function that represents the initial population in the X state is assumed to be the harmonic ground state, i.e.,

$$\Psi_{gr}(\mathbf{R},\theta) = \left(\frac{\alpha_R}{\pi}\right)^{1/4} \exp\left[-\frac{\alpha_R}{2}(R-R_0)^2\right] \left(\frac{\alpha_0}{\pi}\right)^{1/4}$$

$$\times \exp\left[-\frac{\alpha_0}{2}(\theta-\theta_0)^2\right], \tag{2.19}$$

where α_R and α_Θ are obtained from the *ICN* stretching and bending force constants,[74] and the equilibrium values of the Jacobi coordinates (R,Θ) are $R_0 = 4.99$ Bohrs, and $\theta_0 = 0.0$ radians, respectively.

The total wave function for the initial state of the system is the product of electronic and nuclear wave functions,

$$\Psi_{0,k}(\mathbf{x},\mathbf{R},\theta) = \sqrt{\frac{2}{\pi}} x_k \exp\left[-\frac{1}{2}(x_1^2 + x_2^2)\right] \mu_k \Psi_{gr}(\mathbf{R},\theta), \tag{2.20}$$

where $\Psi_{gr}(\mathbf{R},\theta)$ is defined by Eq. (2.19) and k denotes the initially populated excited electronic state. The electronic wave function in Eq. (2.20) is a product of one dimensional harmonic oscillator wave functions, since these are the eigenfunctions of the part of the quantum Hamiltonian that models the electronic degrees of freedom [cf. Eq. (2.6)]. The electronic wave function for state k is a ground state harmonic oscillator wave function for all electronic modes except the kth one, which has one quantum of excitation.

III. RESULTS

Results are presented in three sections. First, Sec. III A presents the semiclassical results for the photoabsorption spectrum compared with that given by full-quantum mechanical calculations. Section III A also shows the comparison between the survival amplitude components obtained according to the semiclassical methodology presented in Sec. II, and the corresponding reference results from full-quantum mechanical simulations. Section III B presents the semiclassical results for the *CN* rotational energy distributions associated with the two possible photofragmentation channels, and the comparison with the corresponding full-quantum mechanical calculations, for photoexcitation to the $^3\Pi_{0+}$ electronic excited state at two different energies. Section III B also presents the comparison of the semiclassical results for the individual wave packet components, in the $K-J$ representation, with the corresponding full-quantum mechanical wave packets in the $^3\Pi_{0+}$ and $^1\Pi_1$ electronic excited states. This complete comparison of the individual wave packet components also provides a comprehensive understanding of the spectroscopic features in the final *CN* rotational distributions. Finally, in order to make a direct comparison between our semiclassical calculations and the classical-analog results obtained by Schatz and co-workers, we present in Sec. III C the rotational distributions, and the wave packets components in the $K-J$ representation, obtained according to the empirical potential energy surfaces developed by Goldfield and co-workers. Full-quantum mechanical results are obtained using the fast Fourier transform (FFT) method with an extended grid of 512 points in both the R and Θ coordinates, defined in the range of coordinates $|R-9|$ a.u. < 5 a.u., and $|\Theta| < 2\pi$ radians.

A. Absorption spectrum and survival amplitude

Figure 5 shows the comparison of the semiclassical results for the total photoabsorption spectrum (solid lines) with the total absorption given by full-quantum mechanical calculations (dashes), as well as the comparison of the semiclassical and the full-quantum mechanical results for the individual absorption components to the $^3\Pi_{0+}$, $^1\Pi_1$, and $^3\Pi_1$ electronic excited states.

The first feature to note in this comparison is that the photoabsorption spectrum obtained according to the SC–IVR methodology presented in Sec. II is in excellent agreement with full-quantum mechanical calculations in terms of the shape and position of the absorption band, not only for the total absorption spectrum but also for each individual contribution to the $^3\Pi_{0+}$, $^1\Pi_1$, and $^3\Pi_1$ electronic excited states. The small differences in the absorption intensities can
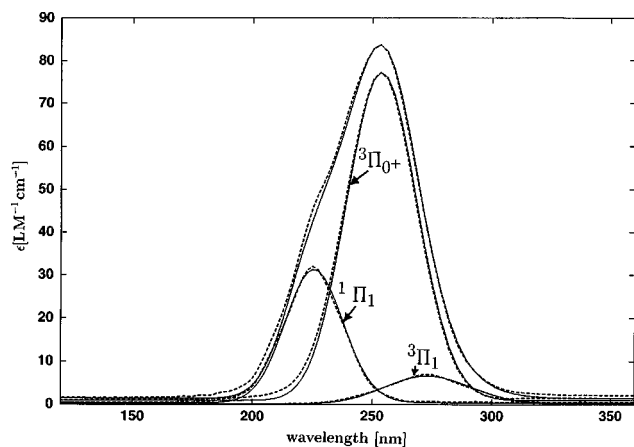
FIG. 5. Comparison of the *ICN* photoabsorption spectrum calculated in terms of the semiclassical methodology described in Sec. II (solid lines), with the corresponding full quantum mechanical results (dashes). Contributions from the individual populated states are also displayed for the $^3\Pi_{0+}$. $^1\Pi_1$, $^3\Pi_1$ electronic excited states.

be traced to small deviations in the survival amplitude envelope, as discussed later in this section. The spectra presented in Fig. 5, obtained according to semiclassical and full-quantum mechanical methods are not only in excellent agreement with each other, but also in very good agreement with the experimental data presented in Fig. 1.

The individual contributions to the absorption spectra, from the $^3\Pi_{0+}$, $^1\Pi_1$, and $^3\Pi_1$ electronic excited states, are obtained as described in Sec. II according to the Fourier transform of the survival amplitudes presented in Fig. 6. In order to check the accuracy and reliability of the semiclassical methodology described in Sec. II, Fig. 6 also compares the real part and modulus of the semiclassical survival amplitudes $\xi(t)$ (solid lines) to the corresponding full-quantum mechanical results (dots). With the exception of small deviations in the shape of the envelope of the survival amplitudes, one sees that the semiclassical results are in excellent agreement with full-quantum mechanical calculations, both in terms of the frequencies and the relaxation times. The ultrafast decay within the first 10 fs after photoexcitation of the system, and the absence of recurrences in the survival amplitudes at longer times, indicate that the photofragmentation process is direct, in the sense that the wave packet moves in the space of nuclear coordinates directly towards dissociation.

Branching processes between the $^3\Pi_{0+}$ and $^1\Pi_1$ electronic state populations becomes significant only after the first 20 fs of dynamics, when the system reaches the conical intersection. Therefore, nonadiabatic couplings have only a minor effect on the absorption spectra, but play a crucial role in determining the branching ratio of photofragment yields and the corresponding rotational distributions of *CN* photofragments.

The semiclassical method for computing the survival amplitude $\xi(t)$, presented in Sec. II, is a direct approach based on Eq. (2.16) which does not require the computation of the time dependent wave function. The survival amplitude results, presented in this section, are converged with 10^6 trajectories integrated according to a standard fourth-order
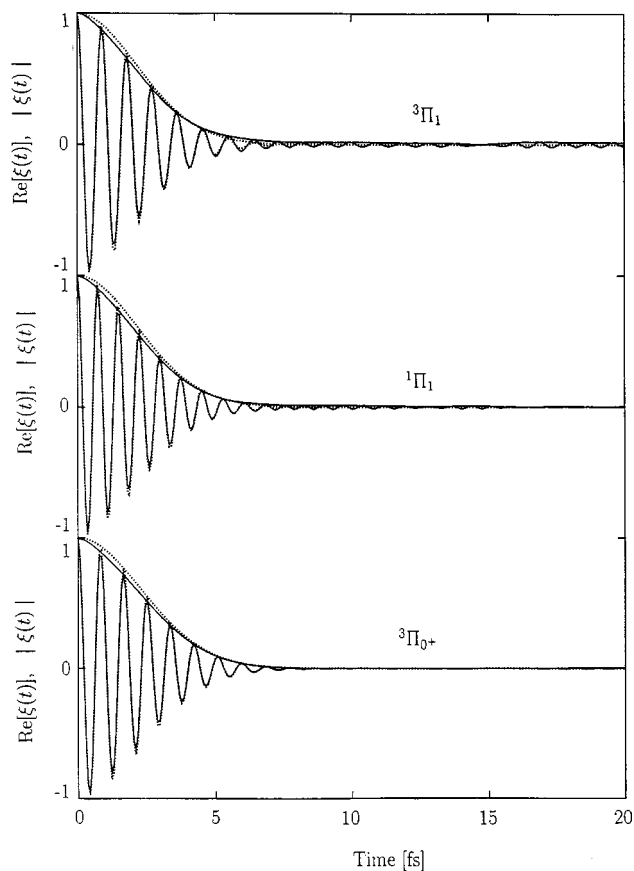

FIG. 6. Comparison of the modulus (long dashes) and real part (solid line) of the survival amplitudes associated with photoexcitation to the $^3\Pi_{0+}$, $^1\Pi_1$, $^3\Pi_1$ electronic excited states, calculated according to the semiclassical methodology presented in Sec. II, with the corresponding full-quantum mechanical results (dots) for the first 20 fs of dynamics.

Runge–Kutta algorithm,[75] using the parallel programming model described in Ref. 2. All forces and second derivatives necessary for integrating the equations of motion presented in Sec. II are calculated using finite difference expressions. The system of two Jacobi coordinates evolving on two electronic surfaces coupled by a conical intersection involves the computation of an eight-dimensional integral with an oscillatory integrand, for which it is necessary to propagate 73 variables that include nuclear and electronic coordinates and momenta, the partial derivatives of each of them with respect to the initial coordinates and momenta, and the classical action. Since most of the degrees of freedom involved in the equations of motion are rapidly changing variables, it is necessary to employ a fairly small integration step $\delta = 0.012$ fs in order for the equations of motion to be integrated accurately, and to reinitialize the stability matrix every 0.12 fs to calculate the partial derivatives at longer times according to the chain rule. The values of the parameters $\gamma(j)$ for the electronic degrees of freedom j are arbitrarily set equal to 1 a.u., while $\gamma(j)$ for the nuclear variables are a set equal to $\alpha(j)/2$, introduced by Eq. (2.19).

B. Nascent *CN* rotational distributions

In order to make a rigorous comparison between the semiclassical and full-quantum mechanical *CN* rotational
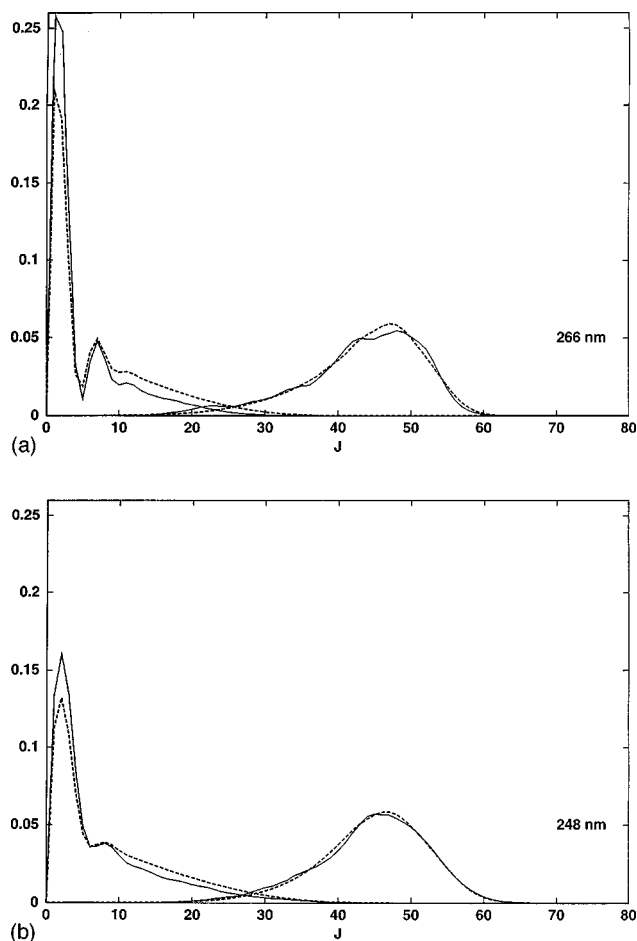
FIG. 7. Contributions of parallel transitions $X \leftarrow {}^3\Pi_{0+}$ to the rotational product distributions at different photoexcitation energies: (a) 266 nm; (b) 248 nm. The solid lines are the semiclassical results obtained as described in Sec. II, using the *ab initio* potential energy surfaces. Dashed lines are the corresponding full-quantum mechanical results.

distributions, Fig. 7 compares the contributions of parallel transitions $X \leftarrow {}^3\Pi_{0+}$ to the total CN rotational distributions at 266 nm, and 248 nm, respectively. The solid lines are the semiclassical results obtained as described in Sec. II, from the time evolved wave function of the system in the $K-J$ representation at 70 fs after photoexcitation of the system. The calculations of the time evolved wave function and rotational distributions were converged with 2×10^7 trajectories, propagated according to the programming model outlined in Sec. III A. The dashed lines are the corresponding full-quantum mechanical calculations. Although the wave function of the system in the $K-J$ representation is not completely in the asymptotic region at 70 fs, it differs only modestly from the fully asymptotic wave function at 200 fs, a time at which the computational cost for totally converging the semiclassical calculations is forbidding.

The semiclassical rotational product distribution associated with the $I^*({}^2P_{1/2}) + CN$ photofragmentation channel has a maximum peak at $J < 5$, and is shown in panels (a) and (b) of Fig. 7 for photoexcitation energies at 266 and 248 nm, respectively. These results are also compared in Fig. 7 to the full-quantum mechanical rotational product distributions associated with parallel transitions, $X \leftarrow {}^3\Pi_{0+}$. Although one

sees that for this photodissociation channel there are some small differences between the semiclassical rotational distributions and the full-quantum mechanical results, the overall qualitative features are in excellent agreement with each other in terms of the shape and position of the band, the shape of the superimposed resonance structure at about $J = 5$, and the trend of these spectroscopic features when the excitation energy is increased from 266 nm to 248 nm—i.e., for both calculations the tail of the rotational distribution becomes wider when the excitation energy is increased from 266 nm to 248 nm, extending out to $J = 40$, while the superimposed resonance structure becomes less prominent due to the increase of amplitude in the rotational distribution.

Figure 7 also shows the semiclassical rotational product distributions (solid lines) associated with the $I({}^2P_{3/2}) + CN$ photodissociation channel, with a maximum amplitude at $40 \leq J \leq 50$ for both photoexcitation energies. These results are also compared to the corresponding full-quantum mechanical rotational product distributions (dashed lines) that result from parallel transitions $X \leftarrow {}^3\Pi_{0+}$. Figure 7 shows that for this other photodissociation channel there is almost quantitative agreement between SC and full-quantum mechanical results at both photoexcitation energies. As mentioned above, we have included in our calculations only the contributions of parallel transitions $X \leftarrow {}^3\Pi_{0+}$, in order to present a clear and rigorous comparison. Therefore, the spectroscopic bands associated with the $I({}^2P_{3/2}) + CN$ photodissociation channel result exclusively from population that crossed from the initially populated ${}^3\Pi_{0+}$ state to the ${}^1\Pi_1$ electronic state at the conical intersection. The agreement observed in this comparison, therefore, validates our semiclassical treatment and demonstrates that the Meyer–Miller Hamiltonian, quantized according to the SC–IVR methodology, describes the *ICN* photodissociation dynamics in excellent agreement with full-quantum mechanical calculations.

In order to present a complete comparison of the SC and full-quantum rotational product distributions at all energies, as well as comprehensive understanding of the spectroscopic features in the final CN rotational distributions, Fig. 8 compares the SC and full-quantum results for the contribution of parallel transitions to the time evolved wave packet in the K-J representation at 70 fs after photoexcitation of the system. These results are presented in panels (a) and (b) in the form of contour plots for the individual wave packet components associated with the populated electronic excited states ${}^3\Pi_{0+}$ and ${}^1\Pi_1$, respectively. Figs. 8(a), and 8(b) also include the elliptical form of the energy contours defined by Eq. (2.18), as a function of K and J at 266 and 248 nm, respectively, and show that the agreement between SC and full-quantum mechanical results observed at these two energies can also be observed at any other photoexcitation energy. The lowest contour line, in Fig. 8(a), shows that there are small differences in the tail of the nuclear wave packet associated with electronic excited state ${}^3\Pi_{0+}$. This feature is consistent with Figs. 7(a) and 7(b), where the tail of the SC rotational distributions are slightly smaller than the full-quantum amplitudes at $J > 10$. The peak in the rotational product distribution, observed in the $J = 1-3$ range in Figs. 7(a) and 7(b), is slightly more prominent for the SC simula-
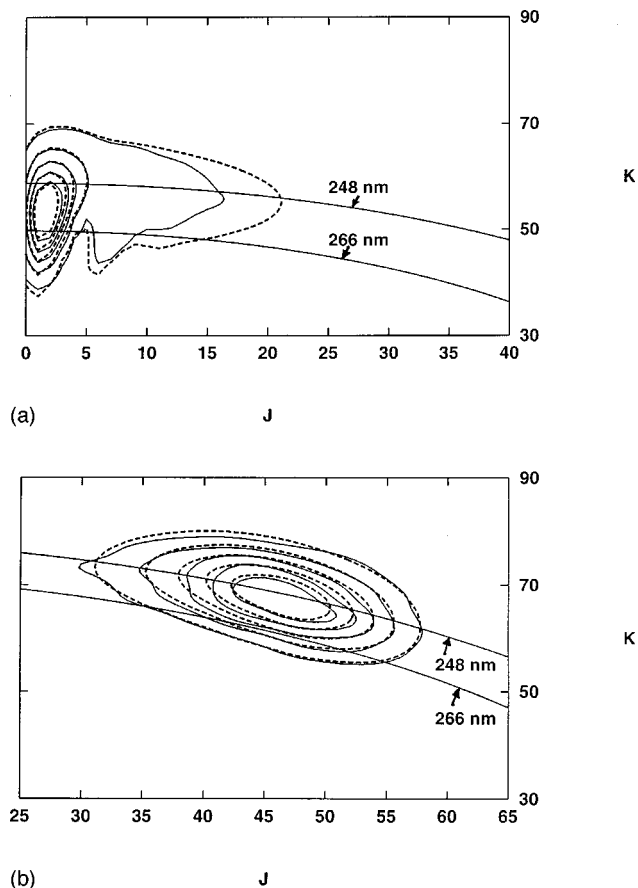
J. Chem. Phys., Vol. 112, No. 13, 1 April 2000

Nonadiabatic photodissociation dynamics   5573

(a)

J

K

(b)

J

K

FIG. 8. Contour plots of the time evolved wave packet in the $K-J$ representation at 70 fs after photoexcitation of the system to the $^3\Pi_{0+}$ electronic excited state, obtained according to the semiclassical methodology presented in Sec. II (solid lines), and the corresponding full-quantum mechanical results (dashed lines). Panel (a) shows the $^3\Pi_{0+}$ wave packet component, and the elliptical form of the energy contour defined by Eq. (2.18), as a function of K and J at 266 and 248 nm, respectively. Panel (b) shows the projection of the $^1\Pi_1$ wave packet component, and the corresponding elliptical energy contour plots as a function of K and J at 266 and 248 nm, respectively.
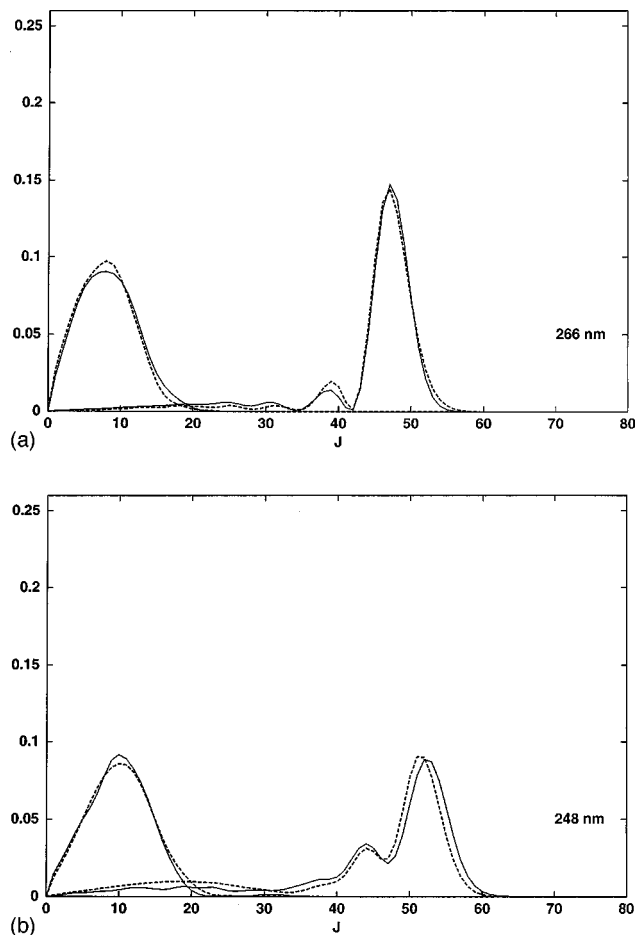
(a)

(b)

J

FIG. 9. Rotational product distributions at different photoexcitation energies: (a) 266 nm; (b) 248 nm. The solid lines are the semiclassical calculations obtained as described in Sec. II, and the dashed lines are the corresponding full-quantum mechanical results, using the empirical potential energy surfaces from Ref. 59.

tions than for the full quantum calculations. This is consistent with the fact that the peak of the SC wave packet is slightly more prominent than the full-quantum mechanical wave packet at these low rotational quantum numbers. Finally, the origin of the resonance feature at about $J=5$, and the trend of this feature as the photoexcitation energy is increased from 266 nm to 248 nm, can be traced to the shape of the wave packet at the intersection with the elliptic energy contour lines at $J=5$ in Fig. 8(a).

The overall agreement between SC and full-quantum mechanical rotational product distributions for the $I(^2P_{3/2})+CN$ channel can also be observed at any other photoexcitation energy, in terms of the shape and position of the band, since there is almost quantitative agreement between SC and full-quantum calculations at all contour lines of the $^1\Pi_1$ wave packet component presented in Fig. 8(b).

C. Results obtained with empirical potential energy surfaces

Figure 9 shows the comparison between the semiclassical rotational product distributions (solid lines) and the cor-

responding full-quantum mechanical results (dashed lines) obtained with empirical potential energy surfaces from Ref. 59, at two different photoexcitation energies. One sees that with exception of small differences the semiclassical rotational distributions are in almost quantitative agreement with full-quantum mechanical results for all populated rotational states of the CN photofragments. Figure 9 demonstrates the capabilities of the semiclassical methodology presented in Sec. II for describing the photodissociation dynamics of ICN according to the empirical potential energy surfaces used in previous theoretical studies, including those presented in Fig. 3.

The semiclassical results presented in this section were converged with 8×10^6 trajectories, after propagating the system for 50 fs according to the programming model outlined in Sec. II A. We find that the empirical potential energy surfaces are significantly different from the *ab initio* potential energy surfaces implemented in Sec. III B, and the wave function of the system in the $K-J$ representation becomes asymptotic in less than 45 fs.

Figure 10 shows contour plots of the time evolved semiclassical wave packet components in the $K-J$ representation at 50 fs after photoexcitation of the system to the $^3\Pi_{0+}$ elec-
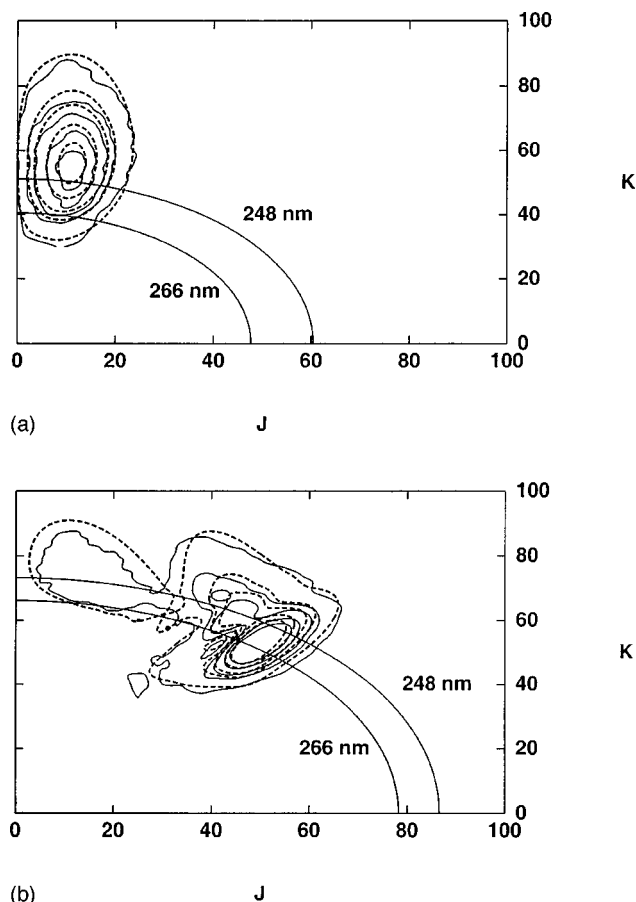
(a)

(b)

FIG. 10. Contour plots of the time evolved wave packet in the $K-J$ representation at 50 fs after photoexcitation of the system to the $^{3}\Pi_{0+}$ electronic excited state, using the empirical potential energy surfaces of Ref. 59. Results obtained according to the semiclassical methodology presented in Sec. II are displayed in solid lines, and the corresponding full-quantum mechanical results in dashed lines. Panel (a) shows the $^{3}\Pi_{0+}$ wave packet component, and the elliptical form of the energy contour defined by Eq. (2.18), as a function of K and J at 266 and 248 nm, respectively. Panel (b) shows the projection of the $^{1}\Pi_{1}$ wave packet component, and the corresponding elliptical energy contour plots as a function of K and J at 266 and 248 nm, respectively.

tronic excited state. Figure 10 also compares the semiclassical results with the corresponding full-quantum mechanical wave packets, together with the elliptical form of the energy contour defined as a function of K and J at 266 and 248 nm, respectively. Figure 10 shows that the agreement between SC and full-quantum mechanical results observed at the two photoexcitation energies presented in Fig. 9 can also be observed at any other photoexcitation energy.

IV. CONCLUSIONS

In this paper we have demonstrated that when the Meyer–Miller classical model for nuclear and electronic dynamics is quantized according to the Herman–Kluk SC–IVR methodology, together with stationary phase MC methods, it describes the *ICN* photodissociation dynamics in excellent agreement with full-quantum mechanical calculations. We have demonstrated the capabilities of the semiclassical methodology by simulating the nonadiabatic photodissociation

dynamics of *ICN* using full *ab initio* PESs, and calculating the *ICN* photoabsorption spectra, and the rotational energy distributions of the *CN* photofragments.

Our SC results are in excellent agreement with full-quantum calculations, demonstrating the potential of this semiclassical methodology for studying reactions involving nonadiabatic complex quantum dynamics in small polyatomic systems. In the spirit of the original formulation of Meyer and Miller, the method treats nuclear and electronic degrees of freedom on the same dynamical footing and involves the propagation of deterministic classical trajectories on an average PES. Here, however, the dynamics is treated within the semiclassical IVR model rather than the more primitive quasiclassical model used earlier. Therefore, quantum coherence is incorporated within this description, and any quenching of interference structure comes about via destructive interference, and no *ad hoc* dephasing approximation needs to be introduced.

ACKNOWLEDGMENTS

[1] W. H. Miller, J. Chem. Phys. **53**, 3578 (1970).
[2] V. S. Batista and W. H. Miller, J. Chem. Phys. **108**, 498 (1998).
[3] V. S. Batista *et al.*, J. Chem. Phys. **110**, 3736 (1999).
[4] V. Guallar, V. S. Batista, and W. H. Miller, J. Chem. Phys. **110**, 9922 (1999).
[5] K. G. Kay, J. Chem. Phys. **100**, 4432 (1994).
[6] K. G. Kay, J. Chem. Phys. **100**, 4377 (1994).
[7] K. G. Kay, J. Chem. Phys. **107**, 2313 (1997).
[8] K. G. Kay, J. Chem. Phys. **101**, 2250 (1994).
[9] A. R. Walton and D. E. Manolopoulos, Mol. Phys. **87**, 961 (1996).
[10] M. L. Brewer, J. S. Hulme, and D. E. Manolopoulos, J. Chem. Phys. **106**, 4832 (1997).
[11] B. E. Guerin and M. F. Herman, Chem. Phys. Lett. **286**, 361 (1998).
[12] M. F. Herman and E. Kluk, Chem. Phys. **91**, 27 (1984).
[13] M. A. Sepulveda and E. J. Heller, J. Chem. Phys. **101**, 8004 (1994).
[14] M. F. Herman and D. F. Coker, J. Chem. Phys. **111**, 1801 (1999).
[15] E. J. Heller, J. Chem. Phys. **94**, 2723 (1991).
[16] E. J. Heller, J. Chem. Phys. **95**, 9431 (1991).
[17] F. Grossmann and E. J. Heller, Chem. Phys. Lett. **241**, 45 (1995).
[18] S. Garashchuk and D. J. Tannor, Chem. Phys. Lett. **262**, 477 (1996).
[19] S. Garashchuk, F. Grossmann, and D. J. Tannor, J. Chem. Soc., Faraday Trans. **93**, 781 (1997).
[20] D. V. Shalashilin and B. Jackson, Chem. Phys. Lett. **291**, 143 (1998).
[21] D. Provost and P. Brumer, Phys. Rev. Lett. **74**, 250 (1995).
[22] G. Campolieti and P. Brumer, Phys. Rev. A **50**, 997 (1994).
[23] G. Campolieti and P. Brumer, J. Chem. Phys. **96**, 5969 (1992).
[24] G. Campolieti and P. Brumer, J. Chem. Phys. **107**, 791 (1997).
[25] W. M. Pitts and A. P. Baronavski, Chem. Phys. Lett. **71**, 395 (1980).
[26] C. J. Williams, J. Qian, and D. J. Tannor, J. Chem. Phys. **95**, 1721 (1991).
[27] J. Qian, C. J. Williams, and D. J. Tannor, J. Chem. Phys. **97**, 6300 (1992).
[28] J. Qian, D. J. Tannor, Y. Amatatsu, and K. Morokuma, J. Chem. Phys. **101**, 9597 (1994).
[29] L. Liu, Jian-Yun Fang, and H. Guo, J. Chem. Phys. **102**, 2404 (1994).
[30] J. M. Bowman, R. C. Mayrhofer, and Y. Amatatsu, J. Chem. Phys. **101**, 9469 (1994).
[31] F. N. Dzegilenko, J. M. Bowman, and Y. Amatatsu, Chem. Phys. Lett. **264**, 24 (1997).

[32] R. Schinke, *Photodissociation Dynamics* (Cambridge University Press, Cambridge, 1993).

[33] H. D. Meyer and W. H. Miller, J. Chem. Phys. **70**, 3214 (1979).

[34] P. Ehrenfest, Z. Phys. **45**, 455 (1927).

[35] W. H. Miller and C. W. McCurdy, J. Chem. Phys. **69**, 5163 (1978).

[36] H. D. Meyer and W. H. Miller, J. Chem. Phys. **71**, 2156 (1979).

[37] H. D. Meyer and W. H. Miller, J. Chem. Phys. **72**, 2272 (1980).

[38] D. A. Micha, J. Chem. Phys. **78**, 7138 (1983).

[39] M. F. Herman and R. Currier, Chem. Phys. Lett. **114**, 411 (1985).

[40] S. Sawada and H. Metiu, J. Chem. Phys. **84**, 6293 (1986).

[41] J. C. Tully, J. Chem. Phys. **93**, 1061 (1990).

[42] J. C. Tully, in *Dynamics on Molecular Collisions, Part B*, edited by W. H. Miller (Plenum, New York, 1976), p. 217.

[43] S. Hammes-Schiffer and J. C. Tully, J. Chem. Phys. **101**, 4657 (1994).

[44] F. Webster, P. J. Rossky, and R. A. Friesner, Comput. Phys. Commun. **63**, 494 (1991).

[45] F. J. Webster, E. T. Tang, P. J. Rossky, and R. A. Friesner, J. Chem. Phys. **100**, 4835 (1994).

[46] D. F. Coker, in *Computer Simulation in Chemical Physics*, edited by M. P. Allen and D. J. Tildesley (Kluwer Academic, Dordrecht, 1993), pp. 315–377.

[47] D. F. Coker and L. Xiao, J. Chem. Phys. **102**, 496 (1995).

[48] V. S. Batista and D. F. Coker, J. Chem. Phys. **105**, 4033 (1996).

[49] V. S. Batista and D. F. Coker, J. Chem. Phys. **106**, 6923 (1997).

[50] V. S. Batista and D. F. Coker, J. Chem. Phys. **106**, 7102 (1997).

[51] I. H. Gersonde and H. Gabriel, J. Chem. Phys. **98**, 2094 (1993).

[52] A. I. Krylov, R. B. Gerber, and V. A. Apkarian, Chem. Phys. **189**, 261 (1994).

[53] A. I. Krylov and R. B. Gerber, Chem. Phys. Lett. **231**, 395 (1994).

[54] S. F. Alberti, N. Halberstadt, J. A. Beswick, and J. Echave, J. Chem. Phys. **109**, 2844–2850 (1998).

[55] K. E. Holdy, L. C. Klotz, and K. R. Wilson, J. Chem. Phys. **52**, 4588 (1970).

[56] U. Halavee and M. Shapiro, Chem. Phys. **21**, 105 (1977).

[57] J. A. Beswick and W. M. Gelbart, J. Phys. Chem. **84**, 3148 (1980).

[58] R. C. Brown and E. J. Heller, J. Chem. Phys. **75**, 186 (1981).

[59] E. M. Goldfield, P. L. Houston, and G. S. Ezra, J. Chem. Phys. **84**, 3120 (1986).

[60] H. Guo and G. C. Schatz, J. Chem. Phys. **92**, 1634 (1990).

[61] H. B. Wang, X. Sun, and W. H. Miller, J. Chem. Phys. **108**, 9726 (1998).

[62] W. T. Pollard and R. A. Friesner, J. Chem. Phys. **100**, 5054 (1994).

[63] J. Shao, L. J. Liao, and E. Pollak, J. Chem. Phys. **108**, 9711 (1998).

[64] X. Sun, H. B. Wang, and W. H. Miller, J. Chem. Phys. **109**, 7064 (1998).

[65] K. G. Kay, J. Chem. Phys. **110**, 8912 (1999).

[66] N. Makri and K. Thompson, J. Chem. Phys. **110**, 1343 (1999).

[67] X. Sun and W. H. Miller, J. Chem. Phys. **110**, 6635 (1999).

[68] G. Stock and M. Thoss, Phys. Rev. Lett. **78**, 578 (1997).

[69] H. Wang, X. Song, D. Chandler, and W. H. Miller, J. Chem. Phys. **110**, 4828 (1999).

[70] V. S. Filinov, Nucl. Phys. B **271**, 717 (1986).

[71] N. Makri and W. H. Miller, Chem. Phys. Lett. **139**, 10 (1987).

[72] J. D. Doll, D. L. Freeman, and T. L. Beck, Adv. Chem. Phys. **78**, 61 (1994).

[73] S. Humbel, S. Sieber, and K. Morokuma, J. Chem. Phys. **105**, 1959 (1996).

[74] G. Herzberg, *Molecular Spectra and Molecular Structure* (Krieger, Malabar, Florida, 1991), Vol. II, p. 174.

[75] W. H. Press, B. P. Flannery, S. A. Teukolsky, and W. T. Vetterling, *Numerical Recipes* (Cambridge University Press, Cambridge, 1986).

[76] W. P. Hess and S. R. Leone, J. Chem. Phys. **86**, 3773 (1987).

[77] I. Nadler, D. Mahgerefteh, H. Reisler, and C. Wittig, J. Chem. Phys. **82**, 3885 (1985).